Nuclear Inst. and Methods in Physics Research, A 1050 (2023) 168178

Contents lists available at ScienceDirect

Nuclear Inst. and Methods in Physics Research, A

journal homepage: www.elsevier.com/locate/nima

Full Length Article

Long term stability studies in the presence of crab cavities and high order multipoles in the CERN super proton synchrotron and high luminosity large hadron collider

A. Alekou [a,b], R.B. Appleby [b,*], E. Cruz-Alaniz [a,c], H. Bartosik [a], M. Carlà [a], S. Kostoglou [a], Y. Papaphilippou [a]

[a] CERN, Switzerland
[b] University of Manchester and Cockcroft Institute, United Kingdom
[c] University of Liverpool, United Kingdom

ARTICLE INFO

Keywords:
LHC
Accelerator
Proton
Aperture
Multipoles

ABSTRACT

In 2018 the world's first Crab Cavity (CC) experiments with protons were successfully performed, aiming to study the CC effect on a proton beam and evaluate the engineering challenges. Before the commencement of these experiments, the impact of the CCs and their multipoles on the long term particle stability of the SPS was studied using dynamic aperture simulations. Furthermore, in order to ensure the long term stability and luminosity performance of the LHC upgrade, the High Luminosity LHC (HL-LHC), the limits of stable motion were also examined in the presence of CC multipole errors, CC voltage errors and additional non-linearities such as the beam–beam effects. This paper presents the comprehensive dynamic aperture results for the SPS and HL-LHC for different CC, accelerator and beam configurations in view of guiding the engineering specifications of the tolerances of the crab cavity multipole errors.

1. Introduction

The upgrade of the Large Hadron Collider (LHC), the High Luminosity LHC (HL-LHC), aims at fully exploiting the LHC physics discovery potential by upgrading the detectors and substantially increasing the LHC luminosity. This upgrade will allow measurements of the Higgs boson properties with unprecedented precision and increase the potential in the search for new physics.

Combined with the upgrade of the injector chain, the HL-LHC aims at a tenfold increase of the integrated luminosity, going from 300 fb^{-1} to 3000 fb^{-1} over a period of 12 years, which implies ~250 fb^{-1} per year. The integrated luminosity $\mathcal{L}_{\mathrm{int}}$ is the integral of the instantaneous luminosity, $\mathcal{L}$, with respect to time: $\mathcal{L}_{\mathrm{int}} = \int \mathcal{L} \cdot dt$, where $\mathcal{L}$ can be expressed as [1]:

$$\mathcal{L} = \gamma \frac{n_b N^2 f_{\mathrm{rev}}}{4\pi\beta^* \epsilon_n} R, \qquad \text{with } R = \frac{1}{\sqrt{1 + \frac{\theta_c \sigma_z}{2\sigma}}}. \tag{1}$$

In Eq. (1), γ is the relativistic gamma factor, n_b the number of bunches per beam colliding at the interaction point (IP), N the bunch population, f_{rev} the revolution frequency, β^* the beam beta function at the IP, ϵ_n the transverse normalized emittance, R the luminosity geometrical reduction factor from the crossing angle (without including the Hourglass effect, and without the CC curvature), θ_c the full crossing angle between the colliding beams (without including the effect of crab cavities) and σ, σ_z are the transverse and longitudinal r.m.s. beam sizes respectively. In the HL-LHC, several upgrades will take place that will enhance the parameters of Eq. (1) [1]. In particular β^* will be reduced from 0.55 to 0.15; this will inevitably result in an increase of the crossing-angle, θ_c, which in turn reduces R from 0.836 to 0.342 (see lower part of Eq. (1)). The most efficient and elegant solution to counteract this effect is the use of special superconducting RF Crab Cavities (CCs), which generate transverse electromagnetic fields rotating each bunch such that there is better overlapping at the IPs of the two experimental detectors ATLAS and CMS. As summarized in Table 1, the CCs allow recovering the luminosity geometrical reduction factor of $R = 0.716$ and the peak luminosity can potentially become more than 10 times higher than the nominal LHC one.

The paper has the following layout: Section 2 describes the CCs, and the necessity to test their validity with protons in the SPS accelerator. The motivation behind the detailed simulation studies presented in this paper is also provided. Section 3 presents the SPS dynamic aperture (DA) simulation studies, i.e. studies concerning the transverse stability of a distribution of particles for a specific number of turns, which are performed with different non-linear fields. The DA studies in HL-LHC

* Corresponding author.
E-mail address: robert.appleby@manchester.ac.uk (R.B. Appleby).

https://doi.org/10.1016/j.nima.2023.168178
Received 16 September 2022; Received in revised form 27 February 2023; Accepted 27 February 2023
Available online 5 March 2023

Table 1
Main parameters for proton collisions in the nominal LHC (design report) and HL-LHC 25 ns (standard) [2,3].

Parameter	LHC	HL-LHC
N [10^{11}]	1.15	2.2
n_b	2808	2748
N_{tot} [10^{14}]	3.2	6.1
Half-crossing angle at IP1 and IP5 [μrad]	142.5	250
Half-crabbing angle at IP1 and IP5 [μrad]	–	190
Minimum β^* [m]	0.55	0.15
ϵ_n [μm]	3.75	2.50
ϵ_L [eV s]	2.50	3.03
R, w/o CCs at min. β^*	0.836	0.342
R, with CCs at min. β^*	–	0.716
$\mathcal{L}_{\text{peak}}$ w/o CCs at β^*_{min} [10^{34} cm^{-2} s^{-1}]	1.00	8.1
$\mathcal{L}_{\text{peak}}$ with CCs at β^*_{min} [10^{34} cm^{-2} s^{-1}]	–	17.0

are described in Section 4, focusing on each individual CC multipole and finding the limit where the long-term stability is affected, in the presence or absence of CC misalignments and beam–beam effects. Finally, the conclusions of these studies are given in Section 5.

2. Crab cavities

The CCs are RF deflecting cavities that give a z-dependent transverse kick to the bunch. Particles at the center of the bunch ($z = 0$) experience no kick, whereas particles at $\pm z = \lambda/4$, where λ is the CC wavelength, experience the largest kick in opposite directions. Since the CC kick is z-dependent, particles at different longitudinal positions will be following different closed orbits and as a result will be experiencing different feed-down errors when passing off-center through the interaction region (IR) elements [4]. A vertical CC kick, y', is given by [5]:

$$y' = \frac{qV_{\text{CC}}}{E}\sin(k \cdot z + \phi), \tag{2}$$

where V_{CC}, k, ϕ, are the voltage, wavenumber and phase of the cavity, and E, z are the energy and longitudinal position of the particle in the bunch respectively. In the HL-LHC, a first pair of CCs will be installed at large β-function locations and with a $\pi/2$ phase-advance from the IPs, so the required CC voltage will be minimized; a second pair will be installed symmetrically after the IPs to close the orbit bump. Note that all CCs will be oriented such that the bunches will be aligned with the z axis and the CC dipolar kick will be in the x or y direction for horizontal or vertical deflection respectively.

The CC designs have converged to two different types: the RF Dipole (RFD) [6] and the Double Quarter Wave (DQW) [7]. The RFD design is expected to be installed at the Interaction Region 1 (IR1) of HL-LHC for horizontal crossing, while the DQW will be installed at Interaction Region 5 with vertical crossing. The imperfections of the CCs can give rise to higher order transverse multipole components that can affect the beam dynamics in the machine (for example by reducing the dynamic aperture). Because of their time-dependent nature, these multipoles are of particular concern (as compared with static multipolar components), as they cannot be corrected by means of traditional magnets. In particular, the tight HL-LHC space constraints lead to axially asymmetric CC designs with enhanced high order multipoles (CC multipoles). Similarly to a dipolar CC field, these multipoles' strengths oscillate with the cavity's frequency and also depend on longitudinal particle position z.

The updated values of the CC multipoles for both designs introduced above up to the octupolar order used in this paper are summarized in Table 2. As described in detail in [8], one can obtain the multipole coefficients, b_n and a_n, using different methods. The values presented in this paper were obtained with the Panowski-Wenzel (PW) method that calculates them via the electric field [4]. Note that the differences in the multipolar values between the two designs, RFD and DQW, as well as in the values used in [4], are a result of the different design

Table 2
Values of vertical CC multipolar components integrated over the cavity length, given in units of 10^{-3} Tm/m^{n-1}, with n defining the multipole order, at the reference deflecting voltage $V_{\text{CC}} = 10$ MV [9].

Multipole	Unit	RFD design	DQW design
b_2 (Q)	10^{-3} T	0	6
a_3 (S)	10^{-3} T/m	−522	1506
b_4 (O)	10^{-3} T/m^2	−914	2106

geometries. In the simulations presented in this paper the multipolar values were scaled according to the CC voltage used.

Although the CCs are expected to increase the luminosity, they also bring several important challenges. The only time CCs were used in the past was with leptons at KEKB in Japan, with which the world's luminosity record was broken in 2009 [10–12]. As the beam size damping from synchrotron radiation is weak in hadron machines (even in the case of the HL-LHC), noise introduced by the CCs (in the form of amplitude or phase jitter) can result in beam degradation such as emittance growth and reduced beam-lifetime. In addition, the CC multipoles, that are time-dependent, will introduce different types of beam dynamics perturbations resulting in resonance excitation, linear tune-shift, chromaticity-shift, chromatic coupling, and amplitude detuning [4]. These optics aberrations will affect the long term stability of the beam.

It was therefore necessary to test the validity of the CC scheme before its installation in the LHC in order to evaluate the CC effect on protons and understand the engineering challenges. With this in mind, a vertical prototype set of HL-LHC CCs (DQW design [13,14]) was installed in the Super Proton Synchrotron (SPS), which served as a test-bed for the world's first CC experiments with protons from April to November 2018. Prior to the CC installation, several machine studies took place at the SPS [15–17] to investigate the natural long-term emittance growth observed in the accelerator in preparation for benchmarking a theoretical model for the emittance growth due to CC amplitude and phase jitter [18]. Furthermore, as the SPS CCs were installed one next to the other, they induced a z-dependent closed orbit distortion ("CC dispersion") around the machine [19]. Therefore, a simulation campaign took place aiming to understand how the long-term stability of the particles is affected in the presence of CC and SPS higher order multipoles. The studies were performed using the concept of DA, i.e. the maximum transverse amplitude below which the particles survive for a specific number of turns similarly to what was done in the past by other studies [20]. Similar studies for the HL-LHC case were executed in order to assure high performance, as additional strong non-linearities, such as the beam–beam effects, could affect the long-term stability of the particles. The main results of the 2018 SPS CC experiments are described in [13].

2.1. Frequency map analysis with crab cavities

As a first step, tracking simulations are employed to compute the Frequency Map Analysis (FMA) as an early indicator of the particles' stability limit [21–24]. A distribution of particles is tracked for 10^4 turns in the SPS lattice with the parameters presented in Table 3 including CCs with 0.5 MV, in the absence of multipoles and in 6D, i.e. considering synchrotron oscillations; the initial $\Delta p/p$ was set to zero whereas the initial z was set to 200 mm. Due to the presence of non-linear chromaticity, the linear chromaticities were adjusted to $Q'_x = 2$ and $Q'_y = 0$ in order to get similar overall chromatic tune shift in the horizontal and the vertical planes. The first and last 5000 turns are used to compute the horizontal and vertical tune of each particle in two time intervals. The tune variation between these two intervals defines the tune diffusion rate.

Fig. 1 illustrates the betatron tunes in the second time span (left) along with the initial horizontal and vertical positions of the particles

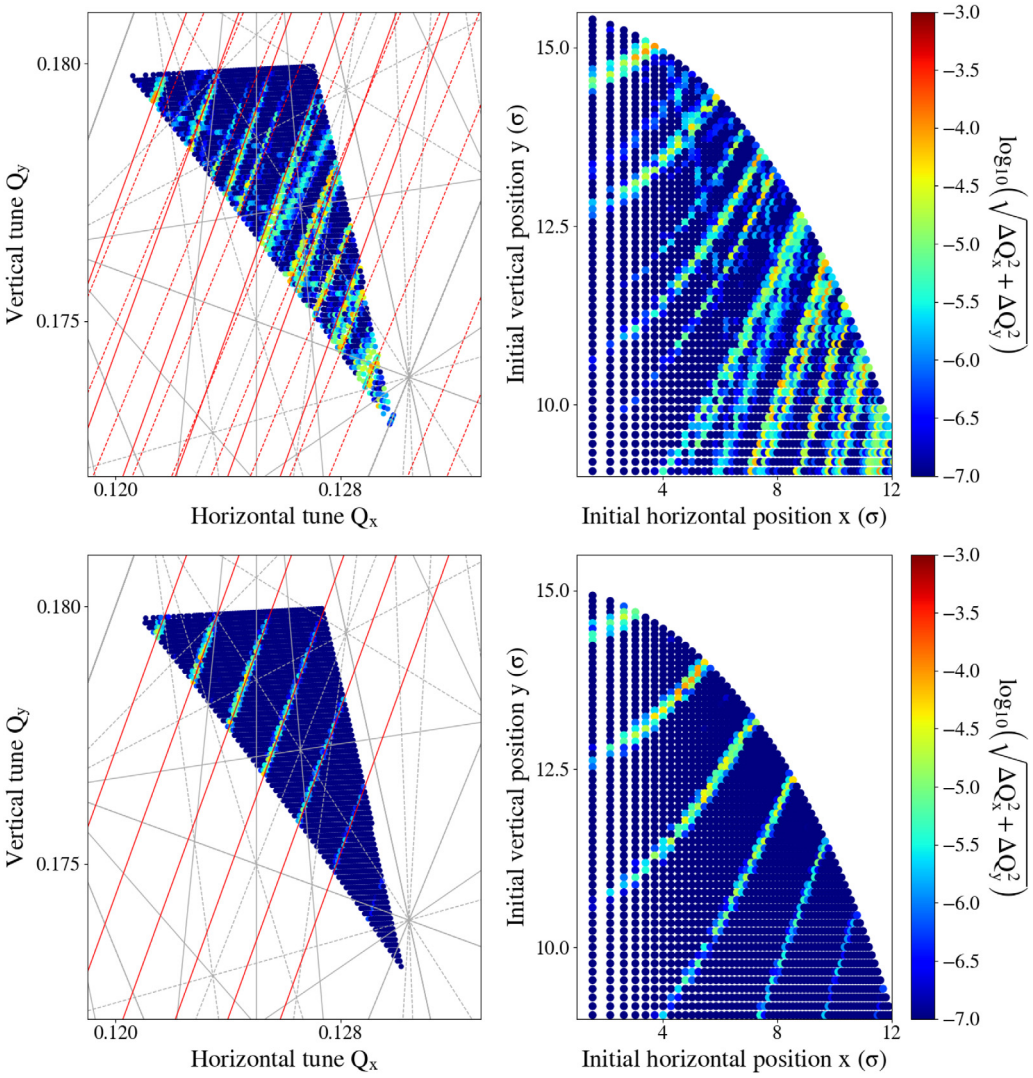

Fig. 1. Frequency Map Analysis (left) and initial horizontal and vertical position (right) with the parameters presented in Table 3, 0.5 MV per CC (top) and without crab cavities (bottom). The color-code illustrates the logarithm of the tune diffusion rate and the gray vertical lines denote the resonance conditions. The sidebands (red), observed even in the absence of CCs (bottom plot), are the synchrotron sidebands that result from the synchro-betatron coupling which comes from the non-zero chromaticity of the machine and the fact that the particles perform synchrotron oscillations.

in the distribution (right) in the presence (top) and absence of CCs (bottom). A color code is assigned to the logarithm of the tune diffusion rate to distinguish particles with stable trajectories (blue) from the ones that encounter resonances (yellow and red) and diffuse. The gray and red lines denote the resonance conditions:

$$k \cdot Q_x + l \cdot Q_y + m \cdot Q_s = n, \tag{3}$$

where k, l, m, n are integers and Q_x, Q_y and Q_s the horizontal, vertical and synchrotron tunes, respectively. The resonance condition described by Eq. (3) includes the effect of tune modulation induced by the coupling of the synchrotron and the betatron motion for off-momentum particles through chromaticity. The chromatic tune modulation results in the excitation of sideband resonances (red) in addition to the ones illustrated with the gray vertical lines [25]. A comparison of Fig. 1 (top) with the frequency map in the absence of crabbing (bottom) yields that the CCs enhance the strength of the sideband resonances.

3. SPS DA studies

The SPS long term stability DA studies were performed using MAD-X [26] and SixDesk [27] without including the actual machine aperture limitations. What the DA estimates is the transverse boundary below which the particles are not lost for a defined number of turns, in this case 10^6, corresponding to 23.05 s. The results are expressed in units of the transverse rms beam-size σ. The SPS parameters at the location of the CCs are given in Table 3. The indices 1, 2 indicate the first and second CC, respectively. 6D tracking simulations were performed for the SPS injection energy, $E = 26$ GeV, as this energy results

Table 3
SPS parameters at the location of the CCs.

Parameter	Value
Number of cavities	2
s-location [m]	6312.7, 6313.3
Transverse tilt [deg]	90
f_{CC} [MHz]	400.528
β_{x1}, β_{y1} [m]	29.2, 76.1
β_{x2}, β_{y2} [m]	30.3, 73.8
Q_x, Q_y	26.13, 26.18
E_{inj} [GeV]	26.0
γ_{rel}	27.7
$\epsilon_{n,x}, \epsilon_{n,y}$ [μm rad]	2.50, 2.50
V_{RF} [MV]	2
Bunch length [m] ($1\ \sigma$)	0.23
ϵ_L [eV s]	0.5

in the largest CC kick, and chromaticities $Q'_{x,y} = 0.0$, using different particle amplitudes with a $2\,\sigma$ step and 5 angles in the initial transverse configuration space (x–y plane), from 15° to 75°. Note that the DA at 0° and 90° was not considered here, since in these cases the particle oscillations are restricted to one plane only, i.e. corresponding to pure horizontal or pure vertical oscillations, respectively [28].

3.1. DA in the presence of CC multipoles

Using only chromatic sextupoles for chromaticity correction and no other optics non-linearities, the DA of the SPS was studied in the presence of CC multipoles using initial $\Delta p/p = 10^{-3}$, and 2 MV per CC resulting in a maximum vertical closed orbit of 0.013 m. This study was done to evaluate the impact of the CC multipoles only and disentangle the effect of feed-down from the rest of the machine non-linearities, therefore none of the latter were incorporated. Furthermore, no physical aperture was included in the simulations. A new generalized RF multipole element was introduced in MAD-X and SixTrack [29,30] to model the CCs and their multipole errors.

Since the SPS experiments were executed for different CC phase configurations, these simulations were performed for a anti-phase mode, where $\phi_1 = 0°$, $\phi_2 = 180°$, and an in-phase mode: $\phi_1 = \phi_2 = 0°$; in the first case the kicks of the two adjacent CCs are cancelled out whereas in the latter they are added. The multipole component was assigned only to one of the CCs so that their effect on the particle stability could be studied independent of the cavity phase settings. For this study the values in Table 2 were used, which are similar to those found in [9]. As the CCs operated in the SPS provide vertical deflection, the quadrupolar and octupolar field errors are transformed to the normal multipoles $(-b_2, b_4)$, whereas the sextupolar errors become skew multipoles (a_3).

Fig. 2 shows the SPS DA when the CCs operate in an anti-phase (top) or an in-phase (bottom) mode. In both plots the black line shows the result when no CCs are present, the yellow line indicates the DA when the CCs are included, whereas for the red, green and blue lines the quadrupolar, sextupolar or octupolar multipole component are added to the first CC, respectively; the purple line shows the result when all three multipole error components are included at the same time. The black dashed horizontal line indicates the physical aperture of $7.6\,\sigma$ (as the CC kick is only acting on the vertical plane only the vertical bottleneck is illustrated). Only the vertical aperture is illustrated.

In the case where the CCs operate in the anti-phase mode (Fig. 2, top), it can be immediately noticed that adding the CCs in the anti-phase mode does not affect the DA. When the multipoles are added the DA only seems to be affected in the case of the skew sextupolar multipole, when on its own (green line) or in combination with the other multipoles (purple line); even then though, the DA is as high as around $40\,\sigma$, and well above the physical aperture.

On the other hand, when the CCs are in-phase (Fig. 2, bottom) the DA reduction is dominated by the non-linear dynamics in the presence of the z-dependent vertical kick of the two cavities adding up, and not by the CC multipoles; this is clear from the fact that the orange line (CCs present, without CC multipoles) overlaps with all other colored lines that include CC multipoles. In this case the DA reduces to about $30-35\,\sigma$ in all transverse angles, a value that is well above the physical aperture of $7.6\,\sigma$. To sum up, these simulations showed that the impact of the CC multipoles on the DA, when used with the baseline values, is minimal.

3.2. Dynamic aperture with respect to the multipolar components' strengths

The above DA results were performed for the baseline multipole values shown in Table 2 [9]. Additional studies investigated the minimum DA for a large range of the multipoles' strengths as presented in the following. All DA studies presented in this paper include the effect of synchrotron oscillations.

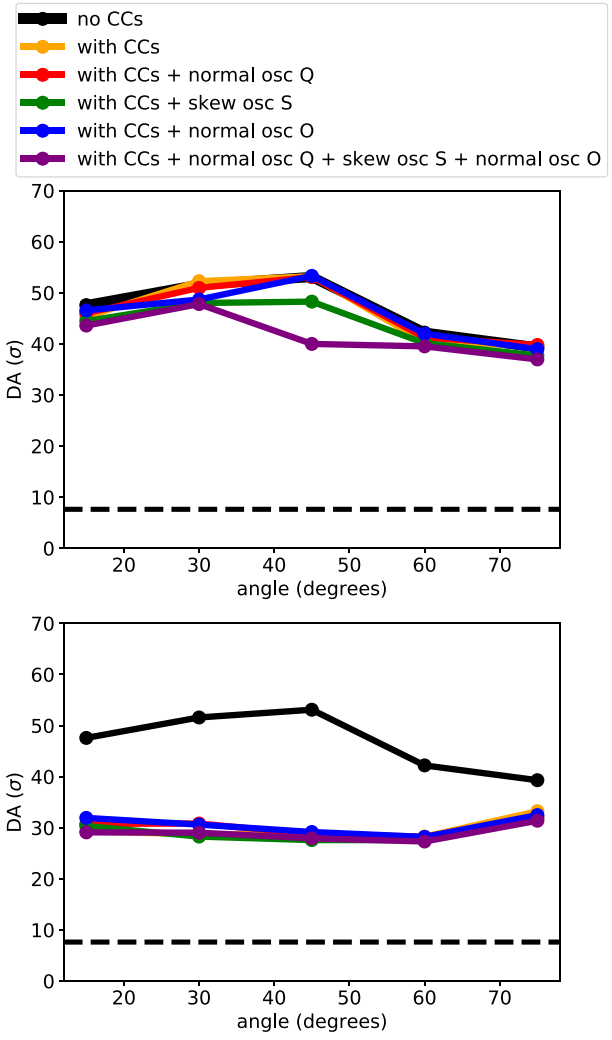

Fig. 2. DA in the SPS in units of σ with respect to the angle in configuration space (0° corresponding to horizontal direction) for the cases where the CCs are in the anti-phase mode (top), i.e. $\phi_1 = 0°$ and $\phi_2 = 180°$, and the in-phase mode (bottom), i.e. $\phi_{1,2} = 0°$; Q: quadrupolar, S: sextupolar, O: octupolar multipoles. The black dashed horizontal line is the vertical physical aperture when no CCs are present ($7.6\,\sigma$).

The minimum DA over all transverse angles for the in-phase CC mode ($\phi_1 = \phi_2 = 0°$), 2 MV per CC and an initial momentum deviation of 10^{-3} is shown in Fig. 3 for different ranges of b_2 (top), a_3 (middle) and b_4 (bottom); the black vertical line indicates the baseline value of the multipoles whereas the horizontal dashed lines illustrate the vertical physical aperture of $7.6\,\sigma$ as calculated at the SPS bottleneck for each case.

As expected, the stronger the multipole value the smaller the DA, however in all three cases multipole errors much higher than the design values need to be employed in order for the DA to be smaller than the physical aperture. In the b_2 and a_3 cases, the DA becomes smaller than the physical aperture for values that are 3 and 2 orders of magnitude larger than the design value, respectively, whereas in the b_4 case this limit is not reached, even for values that are 3 orders of magnitude larger than the design value. As a conclusion the stability limit of the SPS is not expected to suffer from the CC multipoles. During the SPS tests of May–November 2018, an experimental effort took place to characterize the CC a_3 component [31], as summarized briefly below.

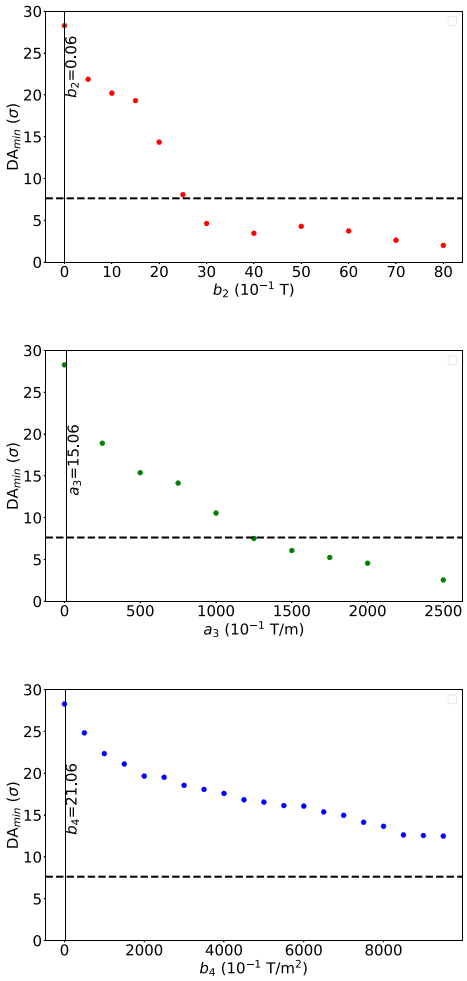

Fig. 3. Minimum DA in σ over all transverse angles, for different values of b_2, a_3, b_4, and $\phi_1 = \phi_2 = 0°$, 10^{-3} initial momentum deviation and 2 MV per CC. The vertical black line shows the baseline value for each multipole and the black dashed horizontal line the physical aperture at 7.6 σ.

3.3. a_3 Measurement

The skew sextupolar (a_3) component is the primary concern for the DQW crab cavity model. While the DQW multipoles composition was studied in detail through electromagnetic simulations, because of the potential impact of such multipoles in terms of the beam dynamics, it was considered necessary to confirm those results with a beam based measurement.

An attempt to measure the a_3 component of the DQW was carried out in October 2018, during the SPS CC tests. The technique of choice relies on the turn-by-turn study of the non-linear betatron motion.

As described in [32], during the SPS CC tests, the magnitude of a_3 was measured for CCs operating at 1 MV each, by exciting the horizontal betatron oscillation and measuring with a turn-by-turn technique the vertical beam motion driven by the skew sextupolar field. As shown in Fig. 4, the vertical motion was thus decomposed in two main contributors: the spectral line $V_{2,0}$, whose frequency is 2 times the horizontal tune, and the spectral line $V_{0,0}$ (a change of the closed orbit), whose frequency is 0. The amplitudes of $V_{2,0}$ and $V_{0,0}$ depend linearly on a_3. Therefore by comparing the turn-by-turn observation of the $V_{2,0}$ and $V_{0,0}$ spectral lines and an analytical model obtained from the first order perturbation theory it was possible to derive the value of a_3. Unfortunately the non-linearities naturally present in the SPS optics combined together with the vertical orbit induced by the CC resulted in the spurious excitation of modes that happen to overlap

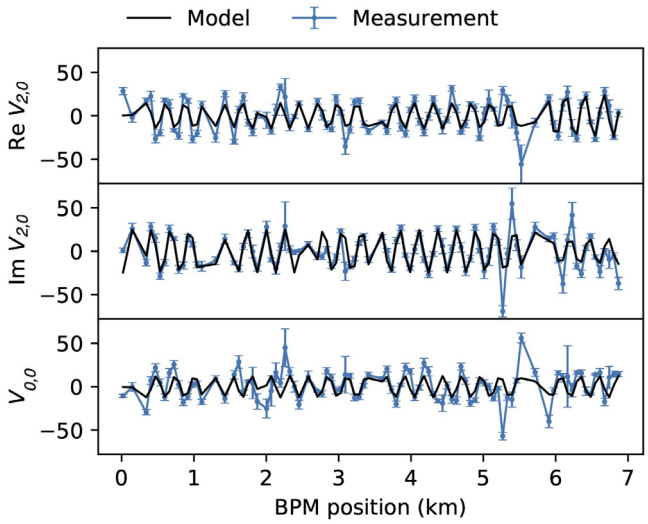

Fig. 4. Variation (blue) of the real and imaginary part of the $V_{2,0}$ spectral line and the $V_{0,0}$ closed orbit distortion induced by changing the CC voltage from 0 MV to around 1 MV per cavity. An analytical model (black) has been fitted in order to establish the magnitude of a_3.

the characteristic ones of the skew-sextupolar multipoles, therefore polluting the results and preventing the determination of a precise estimation of a_3. Nevertheless the measurement was able to restrict a_3 to values ranging from −0.26 T/m to 0.86 T/m, to be compared to the value of 0.3012 T/m obtained from electromagnetic simulations (equivalent to the value of 1.506 T/m for a reference deflecting voltage of V_{CC} = 10 MV mentioned in Table 2).

3.4. DA in the presence of SPS non-linearities

The simulation results presented in Sections 3.1 and 3.2 do not include any non-linear fields of the SPS lattice other than the sextupoles used for chromaticity correction. A dedicated measurement campaign was required in order to consolidate the SPS non-linear model. In fact, during the design and construction phases of the SPS, only a few measurements of the magnets were carried out, focusing especially on the dipoles [33]. The main purpose at the time was to achieve the specified integrated dipolar field, aiming to reduce the closed orbit distortion, while the field flatness and harmonic errors were not of main concern. To improve the knowledge of the non-linear model, beam based measurements have been attempted in the past [34,35] by combining chromaticity scans obtained with two different optics configurations with largely different dispersion functions in order to infer the strength of the various families of multipolar errors. In 2017, a thorough measurement campaign, also based on chromaticity scans, was carried out, this time including a third optics configuration and collecting an overall wider set of measurements.

To match the beam cross section to the magnetic aperture, two different types of dipoles are used in the SPS, referred to as MBA and MBB, respectively. The initial specifications for the SPS dipoles called for a tolerance on the field flatness of about 0.01 % (for MBA and MBB), given the large number of dipoles in the SPS, a non-negligible optical aberration induced by the higher order multipoles in the dipoles is to be expected. The horizontal mirror symmetry of the SPS dipoles does not allow for even multipoles, therefore only odd multipoles are considered in this study.

In order to disentangle the contribution of the different multipolar errors families, a chromaticity scan was repeated for 3 different optics (Q20, Q22, Q26). These optics happen to exhibit a very distinct dispersion pattern as shown in Fig. 5. The measured chromaticity is equal to the sum of the contribution of each multipole weighted by the

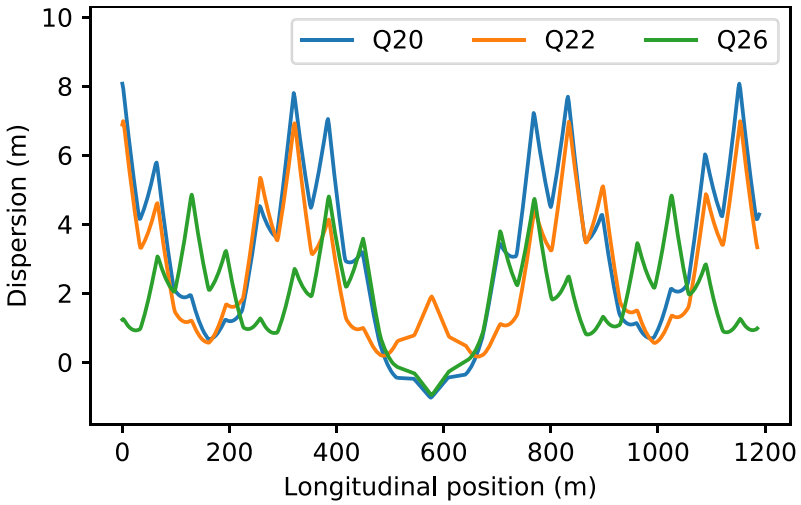

Fig. 5. Horizontal dispersion function for the Q20, Q22 and Q26 optics in one sextant of the SPS. In a chromaticity scan, the different dispersion pattern of the 3 optics results in a different weighting of the non-linearities in the ring.

dispersion. As a result, the non-linearities at different locations in the ring are sampled with different weights depending on the optics due to the fact that the dispersion is different across the ring for each case.

A fitting procedure over the 3 chromaticity scans (one for each optics) allows one to disentangle to some extent the contribution of each error family. For this purpose, the MAD-X/PTC software is used to compute the contribution of each family to the chromaticity. One by one each error family at a time is introduced in the MAD-X model, and a chromaticity scan is simulated by computing the tune for different energy offsets.

The tune shifts with respect to the plain model are arranged in a response matrix $R^o_{\delta,i,p}$, where δ represents the energy offset, i is an index representing each multipole, o indicates the used optic among Q20, Q22 and Q26 and p denotes the horizontal or vertical plane. Given a set of chromaticity measurements for the Q20, Q22 and Q26 optics, the strength of each error family m_i is obtained from the experimental data, with a least square fit procedure, by optimizing the set of parameters m_i, q^o_p to minimize the residual ξ:

$$\xi = \sum_{o,i,p,\delta} [Q^o_{\delta,p} - m_i \cdot R^o_{\delta,i,p} - q^o_p - \delta \cdot \xi_p]^2 \tag{4}$$

where $Q^o_{\delta,p}$ is the tune measured during the three chromaticity scans, while the terms q^o_p and ξ_p have been added to take into account the machine tune and chromaticity settings used during each specific measurement.

Producing an accurate picture of the non-linear behavior of the optics through chromaticity scans requires sampling large dp/p offsets in order to steer the beam up to the very extremes of the horizontal space, where the chromaticity departs strongly from the linear behavior. On the other hand, a good tune measurement can be achieved only as long as the bunch moves coherently like a single particle, a condition that is easily violated due to the decoherence induced by chromaticity along with the non-negligible momentum spread. While it is possible to lower up to a certain extent the linear chromaticity with a proper sextupoles setting, at the very extremes of the dp/p scan chromaticity will naturally diverge due to the same optics non-linearities that are under study here. Therefore, to keep the decoherence under control, it is mandatory to minimize the beam momentum spread, which was achieved by lowering the RF voltage. A total voltage of 300 kV was used, a value that is one order of magnitude smaller than the nominal SPS working condition. A low bunch intensity of about $2 \cdot 10^{10}$ protons allowed beam instabilities to be avoided during machine operation. This intensity is far too low for the SPS beam position monitors (BPM) to provide a reliable measurement, while the Base-Band Tune Meter (BBQ [36]) can still operate. Fig. 6 shows the spectral analysis of the betatron motion continuously exited by the stripline during the entire machine cycle measured with the BBQ.

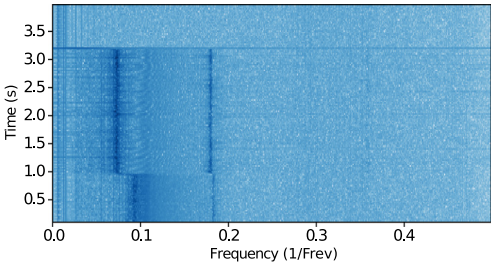

Fig. 6. Spectrum of the horizontal turn-by-turn data acquired with the BBQ BPM during one entire cycle. The beam is injected at the nominal energy and after about 1 s the energy is shifted to the value required by the chromaticity scan. The tune is estimated by averaging the observed peak position during the 2 s interval following the energy shift.

A measurement of the beam momentum is also necessary to estimate the chromaticity, this was derived from the RF frequency by means of the relation:

$$\frac{\Delta p}{p} = \frac{\Delta f}{f} \cdot \left(\frac{1}{\gamma_t^2} - \frac{1}{\gamma^2} \right)^{-1}$$

where γ is the beam relativistic gamma factor and γ_t is the gamma computed at transition crossing. It is worth noting that, while the measurement of f is extremely precise and reproducible, the same does not apply to γ and γ_t, whose estimates rely on the optics model, thus resulting in a potential source of systematic errors. On the other hand, since the SPS linear model is well established, the values of γ and γ_t were assumed to be the nominal ones.

Fig. 7 shows the results of a typical chromaticity measurement for the 3 different optics, along with the result of the multipoles fit. A comprehensive list of the multipolar error families obtained from the collected chromatic detuning measurements is shown in Table 4; in particular a systematic set of multipole errors was assigned to the two types of bending magnets (MBA and MBB) referred to as b_{na} and b_{nb}, respectively, where n is the order of the normal multipole. With this non-linear SPS model, a series of DA simulations was performed to provide more realistic results.

Table 4
Fit of the multipoles included in the SPS non-linear model. The fit is obtained from a combined fit for the 3 optics (Q20, Q22, Q26).

Normal multipole b_n	Unit	Value @ 26 GeV
b_{3a}	T/m^2	$(-2.8 \pm 0.6) \cdot 10^{-3}$
b_{3b}	T/m^2	$(1.6 \pm 0.3) \cdot 10^{-3}$
b_{5a}	T/m^4	-7.9 ± 0.5
b_{5b}	T/m^4	-6.8 ± 1.5
b_{7a}	T/m^6	$(8.8 \pm 2.6) \cdot 10^4$
b_{7b}	T/m^6	$(1.7 \pm 0.8) \cdot 10^5$

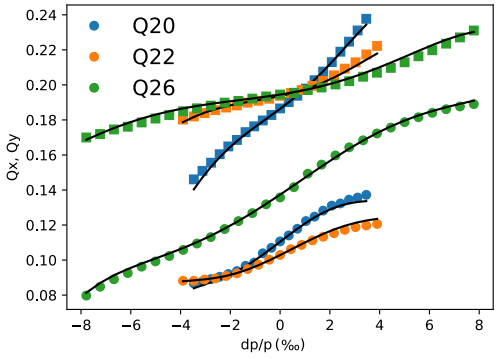

Fig. 7. Horizontal (dots) and vertical (square) fractional tune measured during a typical momentum scan for Q20. Because of the different dispersion in the 3 optics, the dp/p range has been adjusted in order to cover a similar radial excursion. The chromaticity computed from the effective model obtained from the fit of the 3 measurements is also shown (black curves).

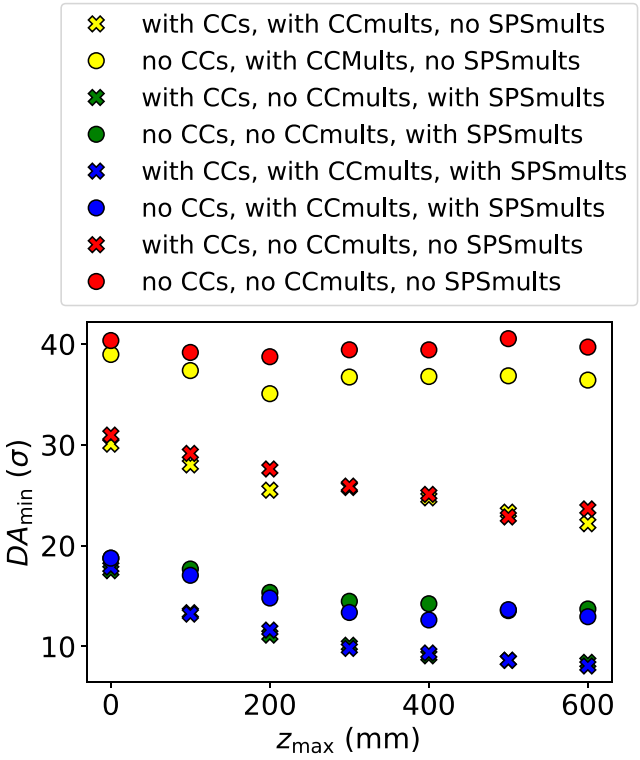

Fig. 8. Minimum DA over all transverse angles for different initial longitudinal actions, z, and initial $\Delta p/p = 0$, in the presence or absence of the CC multipoles or SPS nonlinearities, when the CCs are switched ON at 2 MV each and with $\phi_{1,2} = 0°$ ("x"-points) and when they are switched OFF (circles).

3.5. DA in the presence of crab cavities

A particle performing synchrotron oscillations will obtain a varying kick from the CC with a sinusoidal dependence on z; the larger the initial longitudinal action is, the larger the range of the CC field the particle will experience. Aiming to understand the stability limit reduction that stems from the machine non-linearities in conjugation with the main and error CC harmonics, the following DA studies were performed in the absence or presence of CCs, CC multipoles (all present or absent, simultaneously) and the SPS nonlinearities of Table 4 up to b_7. The simulations were performed for 10^6 turns with the CCs being in-phase ($\phi_1 = \phi_2 = 0°$). To vary the longitudinal action, the initial z was varied from 0 up to 600 mm (i.e. close to a bunch length of $3\,\sigma$), while keeping the initial $\Delta p/p$ at 0. In this way, the DA dependence on the maximum longitudinal excursion, which is now directly obtained, can be better illustrated.

Fig. 8 summarizes the result of the minimum DA for different initial z obtained in different conditions. The case when the CCs are switched OFF, and no CC multipoles or SPS nonlinearities are present, is the reference one (red circles). When only adding the CC multipoles (yellow circles), it can be seen that the DA is not affected, something that was expected from the results shown in Fig. 2. When instead only the SPS multipoles are included (CCs OFF, no CC multipoles), as shown in green circles, the DA is reduced drastically, from around $40\,\sigma$ (red circles) to around $20\,\sigma$ at $z = 0$ mm and to around $15\,\sigma$ at $z = 600$ mm, demonstrating the large effect of the SPS nonlinearities; as expected, no significant change is observed when also including the CC multipoles (blue circles). The strong effect of the CCs on DA can be clearly seen when switching the two CCs ON at 2 MV each while the CC multipoles and SPS non-linearities are absent: the DA decreases from around $40\,\sigma$ when the CCs are OFF (red circles) to around $30\,\sigma$ for $z = 0$ mm and to around $25\,\sigma$ for $z = 600$ mm when the CCs are ON (red "x"-points). As in the case where the CCs are OFF, the addition of CC multipoles does not affect the DA when the CCs are ON (yellow "x"-points). On the other hand, with the SPS machine multipoles included the DA is not affected much when switching ON the CCs irrespective of the presence of the CC multipoles (green and blue "x"-points): a DA reduction of maximum $5\,\sigma$ at $z = 600$ mm is observed, compared to the case where the CCs were OFF (green and blue circles); the most realistic scenario corresponds to the case with CCs on and including the SPS machine nonlinearities and the CC mulitpoles (blue "x"-points).

Fig. 9 shows the minimum DA as a function of the maximum z for the more realistic scenario, i.e. when all the CC multipoles and SPS nonlinearities (up to b_7) were included, for different CC voltages ranging from 0 to 2.5 MV per CC; the initial $\Delta p/p$ was set to 0. The colored lines indicate the available physical aperture in units of vertical σ at the SPS aperture bottleneck taking into account the CC induced closed orbit variation. The black points illustrate the DA when the CCs are OFF (0 MV), or in other words, the limit of stable particle motion in the SPS. The DA decreased gradually with increasing CC voltage and with the longitudinal oscillation amplitudes. This decrease of DA could be relevant for the SPS beam parameters expected at injection energy, where the rms bunch length is typically 23 cm and thus a large fraction of the beam is concerned. On the other hand, it should be emphasized that even for the largest z and the highest simulated voltage of 2.5 MV per CC (note that during the SPS experiments the maximum operational voltage per CC was 1 MV), the particles are limited by the physical aperture and not by DA, which is a very important result for the experimental studies with CCs in the SPS.

4. HL-LHC DA studies

From the SPS results presented in Section 3 it was shown that the SPS limits of stability can be significantly affected when the CCs are used in the presence of non-linear fields (see Fig. 9). In the HL-LHC case, apart from the CC and accelerator nonlinearities, the strong beam–beam effects will be another source of non-linear fields that, in combination with the CCs, could affect the long term stability of the

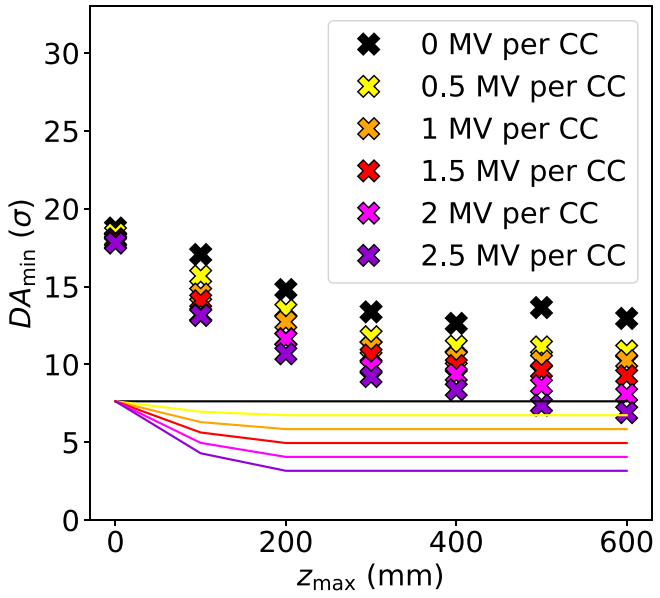

Fig. 9. Minimum DA over all transverse angles for different initial longitudinal positions, z, and CC voltage ($\phi_{1,2} = 0°$), with initial $\Delta p/p = 0$, in the presence of CC multipoles and SPS nonlinearities; the available physical aperture taking into account the crabbing of the beam is indicated by the colored lines.

Table 5
HL-LHC parameters at the location of the CCs.

Parameter	Value
Number of cavities	2 per beam per IP side
CC distance to IP, left [m]	158.6
CC distance to IP, right [m]	154.8
Transverse tilt [deg]	90
f_{CC} [MHz]	400.528
β_x, β_y [m] left CCs	3625, 3712
β_x, β_y [m] right CCs	4279, 3804
Q_x, Q_y	62.31, 60.32
E_{inj} [GeV]	7000
γ_{rel}	7460.5
$\epsilon_{n,x}, \epsilon_{n,y}$ [μm rad]	2.50, 2.50
V_{RF} [MV]	10.2
Bunch length [m] (1 σ)	0.075

proton beam. With this in mind, further studies were performed to evaluate the effects of CCs and their multipoles on the HL-LHC DA.

The studies that follow have a few key differences compared to the SPS case: in the HL-LHC there are two CCs per beam on either side of the IP (i.e. 16 CCs in total); two CC models are used at the main interactions regions: the RFD at IR1 with horizontal crossing, and the DQW at IR5 with vertical crossing; finally, the maximum cavity voltage used is 3.4 MV per CC. Table 5 presents the key HL-LHC parameters at the CC-locations.

Previous HL-LHC DA studies were performed using an earlier version of the CC model (4ROD) [4]. Complementary studies also recommended the reduction of the sextupolar component to less than 1.0 T/m to relax the orbit misalignment to 1 mm and the tolerance for the higher order values to be below 10^n mTm/m^{n-1} [37]. Several changes have been implemented on the operational scenario since these previous studies: the crossing plane has changed to horizontal in IR1 and vertical in IR5 and the crossing angle from 590 μrad to 500 μrad; and finally, a series of changes from the HLLHCV1.1 (used for previous studies [4]) HL lattice version [38], to the one used for these studies (HLLHCV1.3 version [39]). These changes include the reduction from three crab cavities per side per beam to two, changing the integrated voltage from 10.2 MV to 6.8 MV. The following sections explain the calculation of RF multipoles for the last designs of crab cavities, their implementation on the HL-LHC lattice, and finally DA studies to observe their impact.

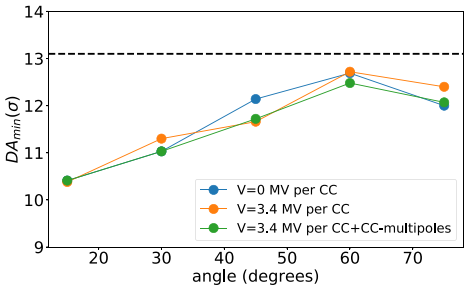

Fig. 10. Minimum DA of 60 seeds vs angle for 0 MV (blue) and 3.4 MV per CC without and with CC multipoles (orange and green respectively). The black dotted lines illustrate the physical aperture (without collimators).

The studies presented in this paper were performed using SixTrack [27] with 10^6 turns, 5 angles in the configuration space (from 15° to 75°), and 6D tracking in the presence of the HL-LHC nonlinearities. As in the SPS case, the CC multipole implementation depends on the crossing at each IR: for the horizontal crossing of the RFD type CCs, the quadrupolar, sextupolar and octupolar components were of type (b_2, b_3, b_4), whereas for the vertical crossing of the DQW type CCs the multipolar components were implemented as (-b_2, a_3, b_4) due to the 90° rotation.

Fig. 10 compares the minimum DA over 60 random number seeds for different angles and for initial $\Delta p/p = 2.7 \cdot 10^{-4}$ when each CC is set to 0 MV (blue) and 3.4 MV without and with the CC multipoles of Table 2 (orange and green respectively), and the physical aperture is also shown for this collision optics at 13.1 σ. A very small effect is observed on the DA when using the CCs and when including their multipoles, and the overall minimum DA stays the same for all three cases. It should be highlighted that the effect on DA is small because the bump created by the CCs is closed; a similar result was observed in the SPS case shown at the top of Fig. 2, as opposed to the bottom plot of Fig. 2 where the CCs were operating in an in-phase mode creating a z-dependent closed orbit distortion (CC dispersion) around the machine.

The following sections focus on each individual CC multipole component aiming to study the limit where the DA starts getting affected, with and without misalignments and beam–beam effects. Note that, at this stage, the misalignments were applied on the plane the CCs have an effect on, i.e. horizontal misalignments are assumed for IR1 and vertical ones for IR5, and they affect the CCs as well as their multipoles.

4.1. Quadrupolar component

As seen in Table 2, the quadrupolar component is zero for RFD and 6 $\cdot 10^{-3}$ T for DQW, at reference deflecting voltage. In this study, the DQW b_2 value was increased, and its effect on DA was calculated for 20 seeds and 5 angles, while the other multipoles, including the zero b_2 in RFD, were kept unchanged. Without the beam–beam effects the DA results, presented in Fig. 11, are similar without and with a 1 mm misalignment (blue and orange respectively), as in both cases the DA reduces by 1 σ at around $100 \cdot 10^{-3}$ T, or about 17 times the nominal b_2 value. Without including any misalignments, as they showed no effect on the DA, the beam–beam effects were incorporated (green line). Both head-on and long-range beam–beam effects were considered, with a β^* = 15 cm at IP1 and IP5 for round optics and at an intensity of $1.15 \cdot 10^{11}$ protons per bunch. For this case the DA is reduced to around 6 σ, which is expected when beam–beam effects are added. A 1 σ DA reduction was only observed at around $180 \cdot 10^{-3}$ T, i.e. around 30 times the nominal value. This result shows that when beam–beam effects are considered, the effect of CC multipoles becomes noticeable only for much higher multipolar values.

As mentioned above, a quadrupolar component is present only in the DQW CC model and not in the RFD. An additional study was

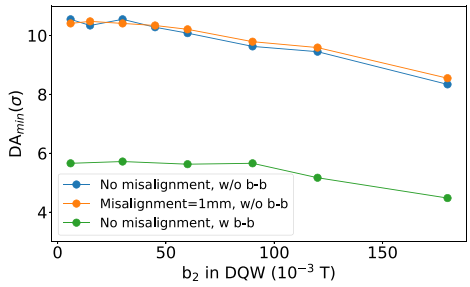

Fig. 11. Minimum DA for 5 angles in configuration space and 20 seeds with increasing b_2 component in DQW in IR5. Cases are shown for: no misalignments and no beam–beam (blue), 1 mm misalignments and no beam–beam (orange), and no misalignments and with beam–beam (green).

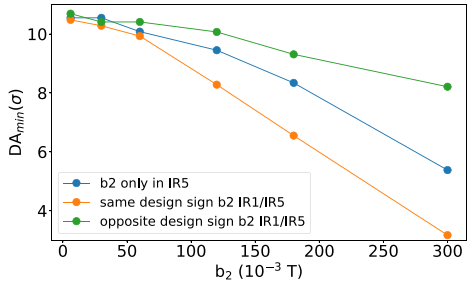

Fig. 12. Minimum DA for 5 angles and 20 seeds with an increasing quadrupolar component only in IR5-DQW (blue); and when including a quadrupolar component also in the IR1-RFD with the same (orange) and opposite (green) sign to the one used in IR5-DQW.

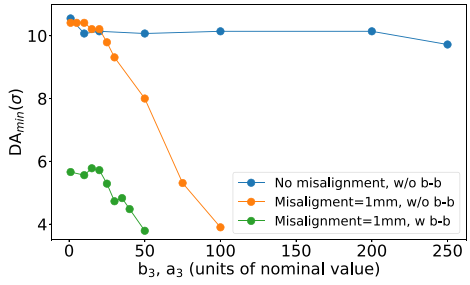

Fig. 13. Minimum DA for 5 angles and 20 seeds with increasing sextupolar component on both DQW and RFD. The effect on DA is shown for the cases with no misalignments and no beam–beam effects (blue), with misalignments of 1 mm and no beam–beam effects (orange), and with misalignments and beam–beam effects (green).

performed to observe how the DA is affected when this component is included in the RFD CC model, and how a change of its polarity further affects the stability limits due to its enhancement or cancellation between the two main IRs. Fig. 12 presents the minimum DA of 20 seeds and 5 angles in configuration space, without including any misalignments or beam–beam effects, for increasing b_2 values and for the case where this component is only present in DQW (blue), as well as in RFD with the same (orange) and opposite (green) design sign to DQW. For small b_2 values the DA results are similar, whereas for larger values it is clear that the DA depends on the sign of the CC multipoles. Note that when the b_2 multipoles have the same design sign, i.e. the opposite effective sign due to the 90° rotation of the DQW cavity (orange line), their effect adds up and the DA decays much faster with a DA reduction of 1 σ at b_2 of around $90 \cdot 10^{-3}$ T. On the contrary, when the multipoles have the opposite design sign, or the same effective sign (green line), the two components cancel out resulting in a more stable scenario, with a 1 σ reduction at b_2 of around $180 \cdot 10^{-3}$ T, and therefore more stable even when comparing with the case when no b_2 units are present in IR1.

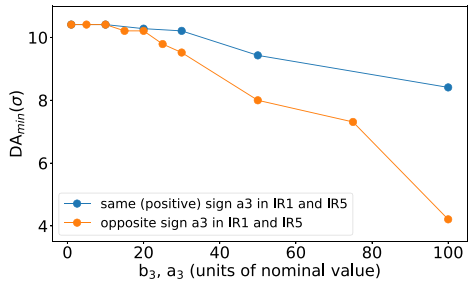

Fig. 14. DA for 5 angles and 20 seeds with increasing sextupolar component when a 1 mm misalignment is included on the CC and its multipoles, for the case with positive sextupolar values in both IRs (blue) and for the reference case with positive sextupolar values at IR5 and negative ones at IR1 (orange).

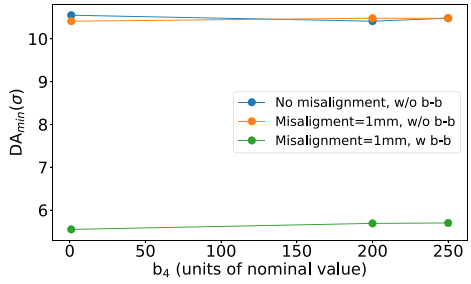

Fig. 15. Minimum DA for 5 angles and 20 seeds with increasing octupolar component on both DQW and RFD. The effect on DA is shown for the cases with no misalignments and no beam–beam effects (blue), with misalignments of 1 mm and no beam–beam effects (orange), and with misalignments and beam–beam effects (green).

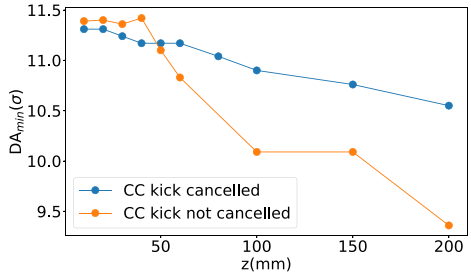

Fig. 16. Minimum DA in the HL-LHC lattice for different initial longitudinal positions. The case where all CCs (left and right at both IPs) are at 3.4 MV (CC kick cancelled out) is shown in blue, and the case where only the CCs on the left of IP1 are set to 3.4 MV (CC kick not cancelled) is shown in orange. For all cases the CC multipoles were included with the nominal values for DQW and RFD; no misalignments and no beam–beam effects were considered.

4.2. Sextupolar component

As with the quadrupolar case, DA studies were also performed for an increasing normal (b_3) and skew (a_3) sextupolar component in RFD and DQW respectively, with and without misalignments and beam–beam effects. Since both CC designs have a non-zero multipolar component ($-522 \cdot 10^{-3}$ T/m and $1506 \cdot 10^{-3}$ T/m at reference deflecting voltage in RFD and DQW respectively), this DA study is performed as a function of the respective sextupolar multipole. The results, illustrated in Fig. 13, show that the DA when no misalignments or beam–beam effects (blue) are included is preserved even for very large values of sextupolar errors. Unlike the quadrupolar case where the DA was similar with and without a 1 mm misalignment, in the sextupolar case the misalignment seems to affect the DA for larger sextupolar values (orange); a 1 σ reduction in DA is observed at around 30 times the nominal sextupolar value which corresponds to $30 - 45 \cdot 10^{-3}$ T/m. Since the misalignments do show an effect on DA, the beam–beam effects were included in

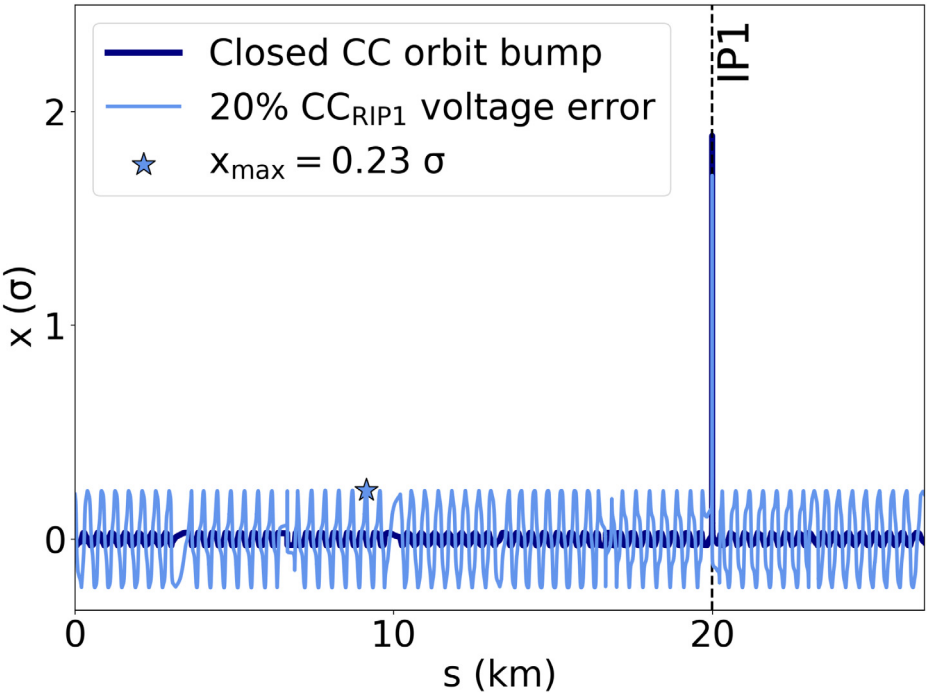

Fig. 17. The horizontal orbit around the ring normalized to the r.m.s. beam size for a particle at z = 75 mm in the presence of a closed CC orbit bump (dark blue) and for a non-closure of the CC bump (light blue) due to an error of 20% in the cavity voltage right of IP1. The maximum orbit excursion due to the orbit leakage (star-shaped marker) and the position of IP1 (black dashed line) are also depicted.

addition (green); similarly to the quadrupolar case, the DA reduces drastically even for the nominal values where a loss of around 5 σ is observed; a 1 σ DA loss is observed at $30 - 45 \cdot 10^{-3}$ T/m, i.e. at the same multipolar value as for the case without beam–beam effects.

In order to explore the effect of the sign difference of the two CC models, the DA was also calculated for positive sextupolar values in RFD, while still including the 1 mm misalignments but omitting the beam–beam effects. The results, presented in Fig. 14, show that when the two multipoles have the same sign (blue) the DA is larger, with a reduction of 1 σ for multipolar values that are around 50 times the nominal value, compared to 30 times for the reference case in which the multipoles have the opposite value (orange); note that this case is the same as the one also depicted in orange in Fig. 13.

4.3. Octupolar component

Further DA studies were performed where the octupolar components were increased for both cavity types. In Fig. 15 it can be seen that the DA for the case without and with 1 mm misalignments (blue and orange respectively) without beam–beam effects is preserved at around 10.5 σ, whereas when the beam-beam effects are included (green) it reduces by about 5 σ. Note that in all three cases the DA is almost unaffected up to about 250 times the reference octupolar values.

4.4. DA dependence on longitudinal position

As shown in Fig. 9 of Section 3.5, changing the initial longitudinal position, z, had a strong effect on the SPS DA. Therefore, this study was repeated for the HL-LHC lattice, where the CC voltage is larger (3.4 MV per CC in comparison to a maximum of 2.5 MV per CC considered in Fig. 9). These studies were done for initial $\Delta p/p = 0$ and including the nominal CC multipoles, as they are shown to have an effect on the HL-LHC DA, but without including any misalignments or beam–beam effects. Note that the HL-LHC 1 σ bunch length is 7.5 cm, therefore this study was performed for a maximum $z = 200$ mm (i.e. close to 3 σ).

The results are shown in Fig. 16. Two cases are presented: the one shown in blue is with all crab cavities (left and right at both IPs) at 3.4 MV, representing the nominal case in which the CC kick is cancelled outside of the IP. The results shown in orange are for the case where only two CCs were set to 3.4 MV (left side of IP1), whereas the other cavities were set to 0 MV. The DA for the case where the CC kick is cancelled out (blue) reduces only by $0.8\,\sigma$ for $z = 200$ mm. The impact on DA is higher for the case where the CC kick is not cancelled (orange), particularly for values of $z > 40$ mm; a reduction of 2 σ is observed at $z = 200$ mm corresponding to less than 20%, i.e. much smaller than the around 50% reduction observed in the SPS case.

4.5. Impact of CC orbit bump non-closure

The $(x - z)$ and $(y - z)$ bunch rotation in IP1 and IP5, respectively, is achieved by installing two CCs on either side of each IP. The CCs generate a closed orbit bump, i.e., the localized perturbation created by the cavity upstream of the IP is compensated by the one downstream and the maximum orbit excursion through the rest of the ring remains unperturbed. However, variations in the nominal CC voltage can give rise to a non-closure of the CC orbit bump. This section investigates the impact of such an effect on the closed orbit, tune diffusion rate and DA.

In the following study, a single beam is tracked (Beam 1) and the weak–strong approximation is used to simulate beam–beam interactions. As a first step, a voltage error is introduced in a single cavity. Using as a reference the clockwise circulation of Beam 1, the perturbed voltage $V_{\rm err}$ of the CC right (downstream) of IP1 due to an error δ is:

$$V_{\rm err} = V_{\rm nom}(1 - \delta) \tag{5}$$

where $V_{\rm nom}$ is the nominal cavity voltage. From the approach adopted in Eq. (5), $\delta = 100\%$ corresponds to a cavity failure scenario while $\delta = 200\%$ yields an inverse CC voltage sign. Although these large values of the voltage errors are beyond the specified tolerances for the HL-LHC, exploring such a regime gives further insight into the repercussions of a CC orbit bump non-closure on the single-particle beam dynamics.

Fig. 17 illustrates the horizontal closed orbit normalized to the r.m.s. beam size for a particle with a longitudinal position z = 75 mm, corresponding to 1 σ r.m.s bunch length, after removing the contribution of the crossing angle. In the presence of a closed CC orbit

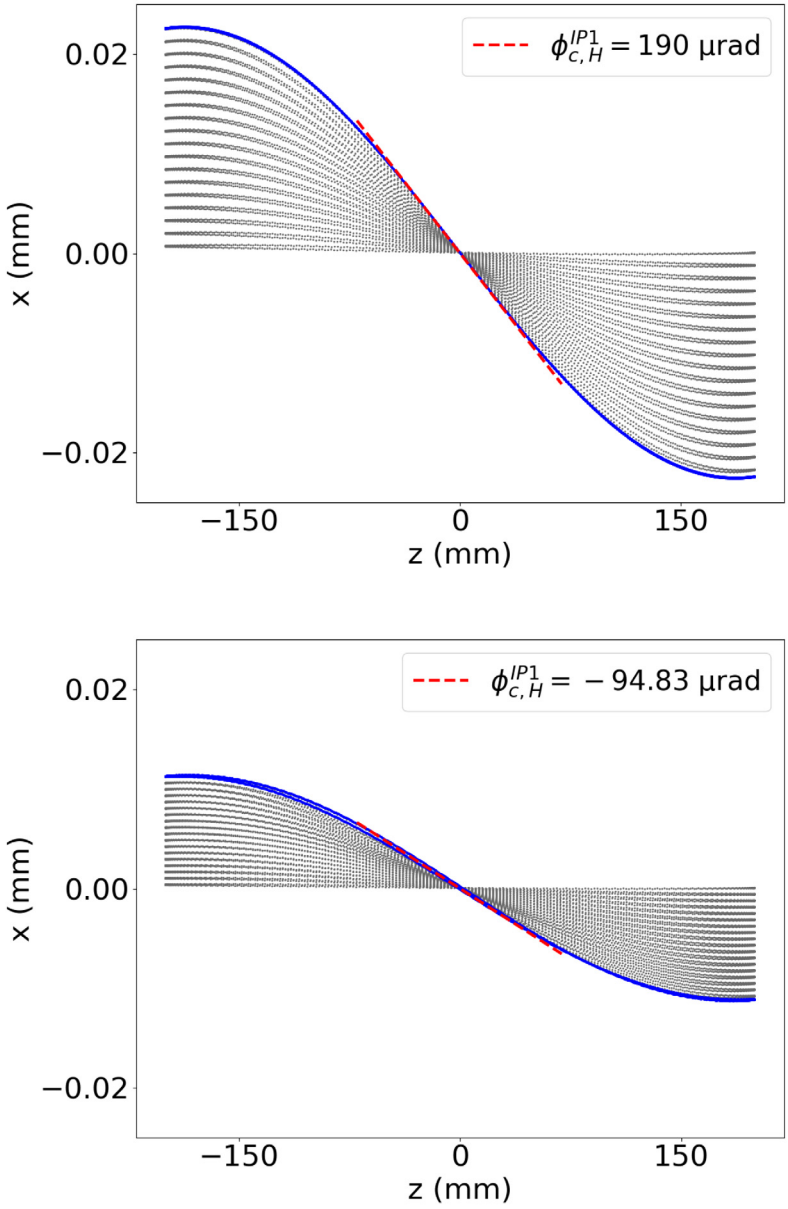

Fig. 18. The turn-by-turn horizontal and longitudinal position retrieved in IP1 for the first (gray) and last (blue) 10^4 turns for a closed orbit bump (top) and an error of 100% in the voltage of the crab cavity right of IP1 (cavity failure scenario, bottom). The linear fit applied to compute the crabbing angle is also depicted (red dashed line).

bump (dark blue), the maximum orbit excursion around the ring is approximately $0.02\,\sigma$. In the linear approximation and for a horizontal crabbing plane, the horizontal position in IP1 (dashed black line) is proportional to the crabbing angle $\phi_{\mathrm{c,H}}^{\mathrm{IP1}} = -190$ μrad and the longitudinal position z.

Next, an error of $\delta = 20\%$ (light blue) is introduced in the voltage of the cavity right of IP1. In this case, the bump non-closure results in an orbit leakage throughout the ring and the maximum orbit excursion increases to $0.23\,\sigma$ (star-shaped marker). The reduction of the horizontal position in IP1 indicates a decrease of the crabbing angle.

Tracking simulations are performed to further evaluate the impact of the orbit non-closure on the crabbing angle. A single particle with an initial longitudinal position $z = 200$ mm is tracked for 2×10^4 turns in the HL-LHC lattice. The turn-by-turn data are collected in IP1 and IP5. An adiabatic ramping of the CC voltage is performed so that the cavities reach their nominal voltage after the first 10^4 turns, which corresponds to 17 synchrotron periods.

The horizontal position x as a function of z collected in the location of IP1 is shown in Fig. 18. The turn-by-turn data acquired prior to and after the completion of the voltage ramp (first 17 synchrotron periods) are depicted with gray and blue, respectively. A linear regression (red dashed) is applied to compute the crabbing angle. Starting from a horizontal crabbing angle of $\phi_{\mathrm{c,H}}^{\mathrm{IP1}} = -190$ μrad in the case of a closed orbit bump (top), the crabbing angle reduces to $\phi_{\mathrm{c,H}}^{\mathrm{IP1}} = -95$ μrad for $\delta = 100\%$ (bottom), which corresponds to a cavity failure scenario. A vanishing crabbing angle occurs for $\delta = 200\%$.

The impact of the orbit non-closure around IP1 on the other IPs is also investigated. The turn-by-turn horizontal and longitudinal positions retrieved in IP5 are shown in Fig. 19 for $\delta = 0$ (black), $\delta = 50\%$ (orange) and $\delta = 100\%$ (green). Although the bunch rotation in IP5 is performed in the vertical plane, the non-closure of the bump in IP1 results in the appearance of an additional bunch rotation in the non-crabbing plane of IP5. A similar effect is also observed in the other IPs.

Voltage errors in the cavities located at both sides of IP1 are considered. Fig. 20 presents the voltage error in the CCs left and right of IP1, spanning from $\delta = 0$ to 20%. For all the possible combinations,

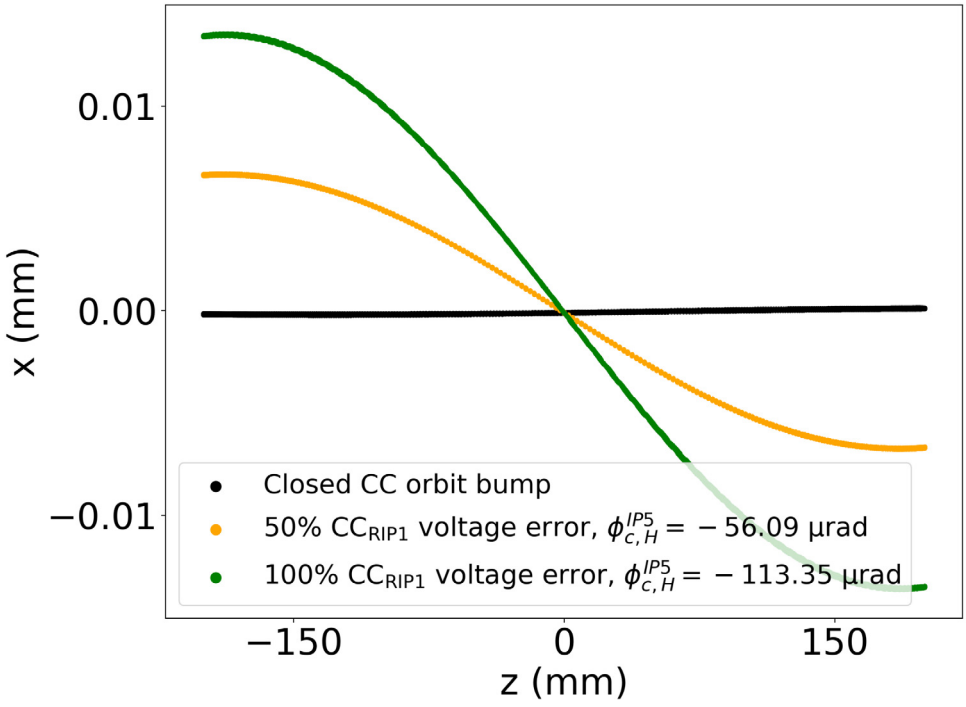

Fig. 19. The turn-by-turn horizontal and longitudinal position retrieved in IP5 for a non-closed orbit bump in IP1 due to a voltage error of $\delta = 0$ (black), $\delta = 50\%$ (orange) and $\delta = 100\%$ (green) in the cavity right of IP1.

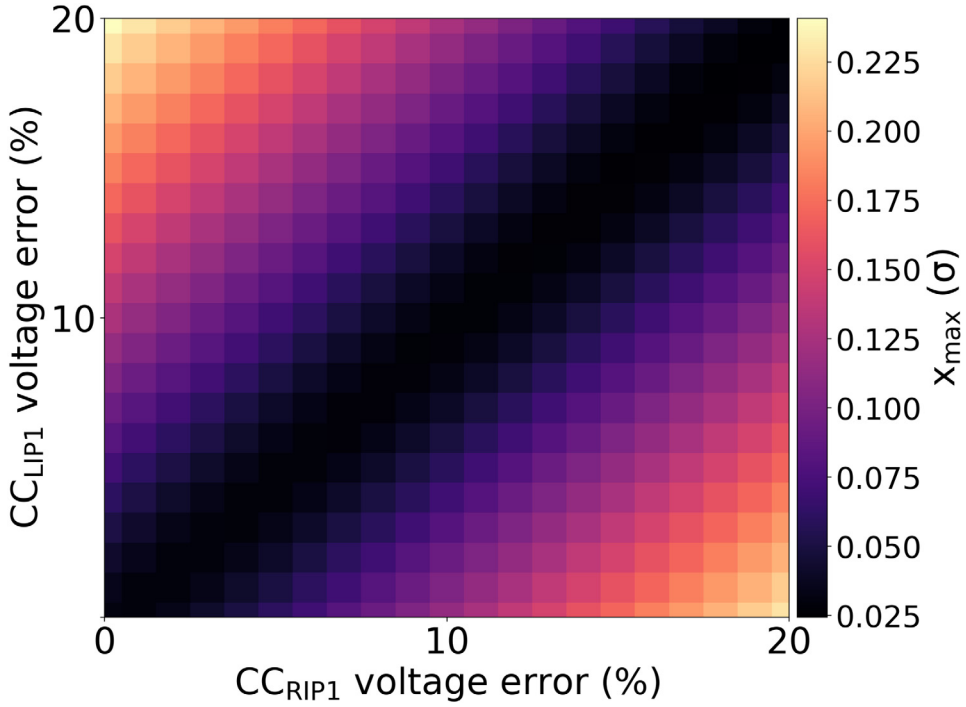

Fig. 20. The voltage error in the CCs right and left of IP1, color-coded with the maximum orbit excursion around the ring for a particle at z = 75 mm. The on-diagonal elements correspond to a closed orbit bump (black) and a reduction of the crabbing angle from its nominal value. The off-diagonal elements (purple to orange) represent the orbit leakage in the ring due to the non-closure of the cavity orbit bump accompanied by a reduction of the crabbing angle.

the maximum orbit excursion through the ring is computed (see star-shaped marker in Fig. 17). A color-code is assigned to its value after normalizing to the r.m.s. beam size. The elements in the diagonal (black) correspond to a closed cavity orbit bump as no orbit leakage is observed through the ring. Nevertheless, the presence of such errors is accompanied by a reduction of the crabbing angle compared to its nominal value. The off-diagonal elements (purple to orange) result in a non-closed orbit bump and an increase of the maximum orbit excursion along with a reduction of the crabbing angle.

The combined effect of the crabbing angle reduction and maximum orbit excursion increase on the long-term beam stability is presented with FMAs. A distribution of particles forming a polar grid in the initial

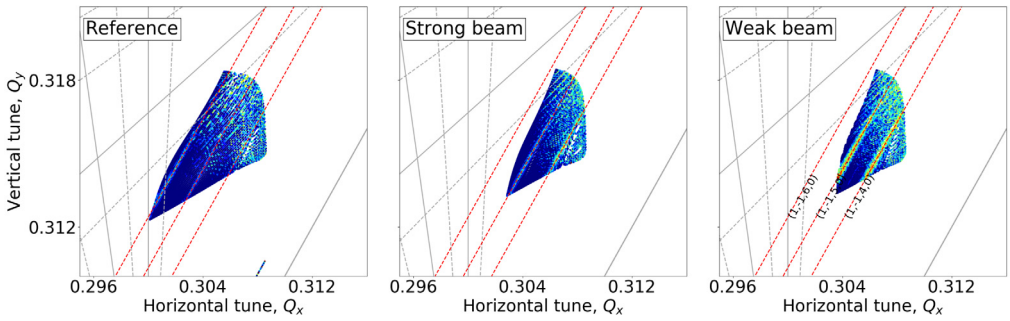

Fig. 21. Frequency Map Analysis for a closed crab-cavity orbit bump (first) and in the presence of a non-closure in the strong (second) and weak (third) beam. The nominal and synchrobetatron resonances are presented with gray and red, respectively.

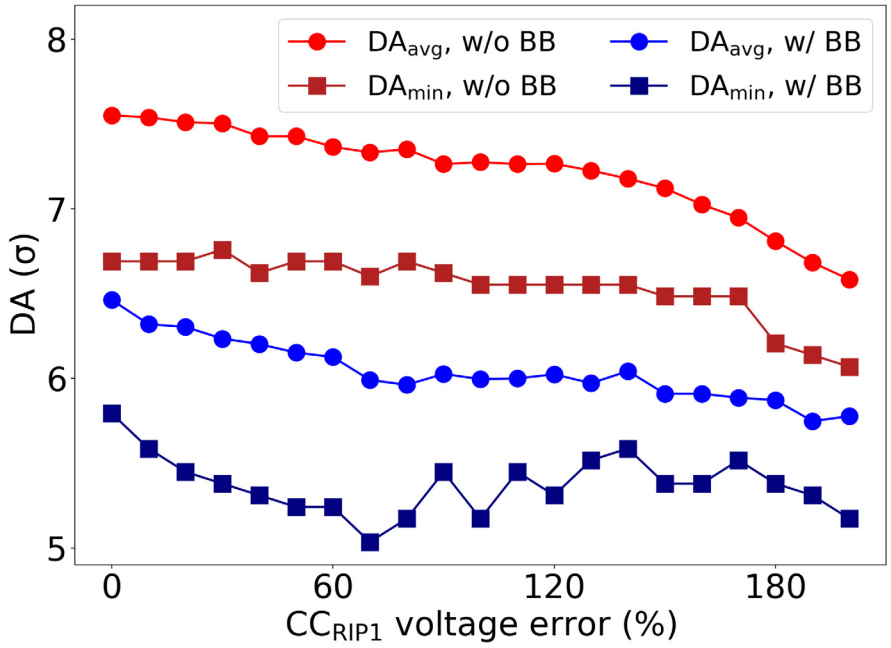

Fig. 22. The average (dark red) and minimum (light red) DA as a function of the voltage error in the CC right of IP1 in the absence of beam–beam encounters. The average (dark blue) and minimum (light blue) DA in the presence of a voltage error in the crab cavities of both the weak and strong beams and in the presence of head-on and long-range interactions.

configuration space with 49 angles and extending up to 6 σ is tracked for 2×10^4, in the presence of beam–beam interactions (only head-on encounters) and taking into account the synchrotron oscillations. Longitudinally, the particles are placed at z = 75 mm.

The studies are organized as follows: first, a voltage error is introduced in the CCs right of IP1 in the lattice of the weak beam (Beam 1) and then, the error is extended to the same element of the strong beam (Beam 2). Although in both cases only the weak beam is tracked, the introduction of such an error in the strong beam affects the weak beam through beam–beam interactions. Specifically, an error in the crabbing of the strong beam yields a change in the beam–beam separation, which is manifested by a modification of the head-on beam–beam lenses, directly impacting the weak beam.

The turn-by-turn data of the last 10^4 turns (after the ramp of the CC voltage) are divided into two groups. The tune of each particle is computed for each time interval and a color-code is assigned to the tune diffusion rate. Fig. 21 depicts the FMAs for a closed cavity orbit bump (first), in the presence of a non-closure due to a cavity voltage error only in the strong (second) and then only in the weak (third) beam. The nominal resonances (gray) and synchrotron sideband (red) are also depicted. Due to the partial rotation of the weak or the strong beam in the IP in the presence of voltage errors, the head-on collisions are only partially restored, leading to a smaller head-on tune spread compared to the reference and thus, improving the long-term stability of the particles. In the case of the weak beam, the non-closure of the orbit bump and the orbit leakage throughout the ring leads to a further excitation of the synchrobetatron resonances. Therefore, the total impact on the long-term stability results from an interplay between the head-on tune spread reduction, which is beneficial for the DA, and the increase of the tune diffusion rate due to the excitation of synchrobetatron resonances that reduces the DA.

DA studies are performed to evaluate the interplay of these two effects. A distribution of particles forming a polar grid with 5 angles and extending up to 10 σ are tracked in the HL-LHC ring for 10^6 turns. The average and minimum DA across all angles of the initial distribution is computed. Fig. 22 presents the minimum (square markers) and the average (circle markers) DA as a function of the voltage error. The studies are organized as follows: first, the beam–beam interactions are not considered (light and dark red). The main contributor to the degradation of the long-term beam stability is the increase of the maximum orbit excursion around the ring. A reduction from 7.5 σ to 6.6 σ and 6.7 σ to 6.1 σ is observed for the average and minimum DA, respectively in the presence of δ = 200% (change of voltage sign).

Next, the beam–beam interactions (both head-on and long-range encounters) are taken into account (light and dark blue) and the voltage error is introduced in the cavities of both weak and strong beams.

Table 6
Summary table of the HL-LHC studies presented in this paper.

Fig.	Study	Mis.	b-b	CC Mult.	1 σ DA reduction
10	DA_{min} vs. angle	N	N	Nominal values	N/A
11	DA_{min} vs. b_2 in DQW	N	N	Nominal a_3, b_4 in DQW and b_3, b_4 in RFD	100 mT in DQW
	DA_{min} vs. b_2 in DQW	1 mm	N	Nominal a_3, b_4 in DQW and b_3, b_4 in RFD	100 mT in DQW
	DA_{min} vs. b_2 in DQW	N	Y	Nominal a_3, b_4 in DQW and b_3, b_4 in RFD	180 mT in DQW
12	DA_{min} vs. b_2 in both DQW and RFD (same sign)	N	N	Nominal a_3, b_4 in DQW and b_3, b_4 in RFD	180 mT in DQW and RFD
	DA_{min} vs. b_2 in both DQW and RFD (opposite sign)	N	N	Nominal a_3, b_4 in DQW and b_3, b_4 in RFD	90 mT in DQW and −90 mT in RFD
13	DA_{min} vs. b_3, a_3 (units of nominal value)	N	N	Nominal b_2, b_4 in DQW and b_4 in RFD	250 × b_3 (a_3): 370,000 in DQW 130,000 in RFD
	DA_{min} vs. b_3, a_3 (units of nominal value)	1 mm	N	Nominal b_2, b_4 in DQW and b_4 in RFD	30 × b_3 (a_3): 45,000 in DQW −15,000 in RFD
	DA_{min} vs. b_3, a_3 (units of nominal value)	1 mm	Y	Nominal b_2, b_4 in DQW and b_4 in RFD	30 × b_3 (a_3): 45,000 in DQW −15,000 in RFD
14	DA_{min} vs. b_3, a_3 (units of nominal value) and changing b_3 sign in RFD to positive	1 mm	N	Nominal b_2, b_4 in DQW and b_4 in RFD	50 × b_3 (a_3): 75,000 in DQW 25,000 in RFD
15	DA_{min} vs. b_4	N	N	Nominal b_2, a_3 in DQW and b_3 in RFD	N/A
	DA_{min} vs. b_4	1 mm	N	Nominal b_2, a_3 in DQW and b_3 in RFD	N/A
	DA_{min} vs. b_4	N	Y	Nominal b_2, a_3 in DQW and b_3 in RFD	N/A

The DA reduction due to the increase of synchrobetatron resonances is compensated by the reduction of the head on tune-spread. As a result, a clear trend in the DA evolution is not observed for voltage errors as high as $\delta = 200\%$. Based on these observations, it is concluded that a non-closure of the orbit bump due to a voltage error in the CCs is not expected to significantly impact the DA and thus, the beam lifetime.

5. Conclusions

This paper presents how the long-term stability of a proton beam is affected by the CCs and their higher order multipoles, for both the SPS and HL-LHC lattices, in combination with accelerator non-linearities, beam–beam effects, and possible CC misalignments using the concept of DA.

The increase in tune diffusion due to the excitation of sidebands resonances in the presence of crab cavities was demonstrated with Frequency Map Analysis. In the SPS case, independent of the CC phase, the presence of CC multipoles when used with their design values did not significantly affect the DA. When the CCs were used in an in-phase mode, values that are 3 and 2 orders of magnitude larger than the design values of the b_2 and a_3 multipole components reduce the DA below the physical aperture. In the b_4 case even for values that are three orders of magnitude larger than the design values the DA is beyond the physical aperture of the machine. As a conclusion the CC multipoles are not shown to have a strong impact on the beam stability in the SPS. DA simulations were also performed for different initial longitudinal positions, z, in the absence or presence of all the CC multipoles and SPS nonlinearities up to b_7, while the CCs were switched ON or OFF. It was shown that, although the CC multipoles do not affect DA, the presence of the SPS nonlinearities reduce the DA by 20–25 σ. Furthermore, when switching ON the CCs in the absence of the SPS nonlinearities the DA reduces by 10–15 σ, whereas in their presence by only 5 σ. Additional studies showed that, in the more realistic scenario where all the CC multipoles and SPS nonlinearities are present, the DA decreases gradually with a CC voltage increase, and this effect is more profound for large z; nonetheless, even for high CC voltages and large z, the beam is not limited by the DA but by the physical aperture. Additionally, to compute experimentally the magnitude of a_3, the two characteristic modes $V_{0,0}$ and $V_{2,0}$ observed in the vertical spectrum were obtained while exciting the horizontal betatron motion. While it was not possible to derive a precise estimation of a_3, it was still possible to restrict the a_3 magnitude to a specific range of values in order to benchmark the theoretical results obtained from electromagnetic simulations.

In the case of HL-LHC, the nominal values of the CC multipoles did not show a significant impact on the DA. Their values were increased to explore tolerances with respect to single-particle stability and it was shown that only two cases were observed where the DA was affected: when increasing the quadrupolar or sextupolar components to values that are about 20 and 30 times the nominal ones, respectively; for the sextupolar case the effect was only observed when considering a misalignment in the CCs. When beam–beam effects were included, the DA reduced drastically by around 5 σ, even for the nominal multipolar values as expected (see [40]), and a 1 σ DA reduction was observed at about 30 times the nominal sextupolar value. It was also shown that in both the quadrupolar and sextupolar cases, the limits on stability change significantly with respect to the sign between CC models. Finally, when including the CC multipoles with their nominal values (no misalignments and no beam–beam) a reduction of up to 0.8 σ for different initial longitudinal actions was observed. The effect is stronger when considering the case where the CC kick is not cancelled (all CCs off apart from the ones on the left side of IR1) with a reduction of about 2.0 σ, which is considerable, although much smaller than the effect observed for the SPS. A non-closure of the CC orbit bump due to the presence of errors in the nominal CC voltage was also considered. The impact of the orbit leakage and the increase of the maximum orbit excursion around the ring, as well as the change of the crabbing angle at the IP and the appearance of a crabbing angle in the non-crabbing plane of the other IPs was evaluated. In the presence of beam–beam interactions, the reduction of the head-on tune spread and the increase of tune diffusion due to the further excitation of synchrobetatron resonances was clearly demonstrated. A comparison of the results from the tracking simulations and the CC voltage error tolerances yields that a non-closure of the CC orbit bump is not expected to significantly degrade the particle stability.

In summary, these studies show that, although the nominal values of CC multipoles do not have an impact on DA, the limits for these values were more strict for the HL-LHC than for the SPS case. On the contrary, when comparing the DA for different longitudinal positions, a large DA effect is observed in the SPS but not in the HL-LHC. The results presented in this paper directly guide the engineering specifications of the tolerances of the crab cavity multipole errors.

Declaration of competing interest

The authors declare the following financial interests/personal relationships which may be considered as potential competing interests: Andri Alekou reports financial support was provided by UK Research and Innovation.

Data availability

Data will be made available on request.

Acknowledgments

The authors would like to thank G. Arduini, R. Calaga, R. De Maria and R. Tomás for the very fruitful discussions and valuable feedback. Research supported by the HL-LHC, United Kingdom project and STFC, United Kingdom through HL-LHC-UK.

Appendix

Table 6 summarizes the HL-LHC studies presented in this paper, specifying if misalignments (Mis.) or beam–beam effects (b-b) are included, and what CC multipoles were considered. Finally, the multipolar value at which the DA is reduced by more than 1 σ is noted.

References

[1] O. Aberle, et al., High-Luminosity Large Hadron Collider (HL-LHC): Technical Design Report, CERN Yellow Reports: Monographs, CERN, Geneva, 2020.
[2] P. Brüning, P. Collier, S. Lebrun, R. Myers, J. Ostojic, P. Poole, O. Proudlock, LHC Design Report, CERN Yellow Reports: Monographs, CERN, Geneva, 2004.
[3] R. Tomas Garcia, et al., HL-LHC run 4 proton operational scenario, 2022.
[4] J. Barranco García, R. De Maria, A. Grudiev, R. Tomás García, R. Appleby, D. Brett, Phys. Rev. Accel. Beams 19 (2016) 101003.
[5] Y. Sun, R. Assmann, J. Barranco, R. Tomás, T. Weiler, F. Zimmermann, R. Calaga, A. Morita, Beam dynamics aspects of crab cavities in the CERN large hadron collider, 2009.
[6] S. De Silva, H. Park, J. Delayen, Z. Li, T. Nicol, Design and prototyping of a 400 MHz rf-dipole crabbing cavity for the LHC high-luminosity upgrade, 2015.
[7] S. Verdú-Andrés, et al., Design and vertical tests of double-quarter wave cavity prototypes for the high-luminosity LHC crab cavity system, Phys. Rev. Accel. Beams 21 (2018) 082002.
[8] E. Cruz Alaniz, Y. Papaphilippou, C. Welsch, RF multipoles deliverable, 2020.
[9] R. Calaga, J. Mitchell, He 152nd HiLumi WP2 Meeting, 2019, Available at https://indico.cern.ch/event/826475/contributions/3457534/attachments/1872608/3082026/WP2_Multipole_Update.pdf.
[10] K. Hosoyama, et al., Development of the KEK-b superconducting crab cavity, in: Conf. Proc. C, 2008, 0806233, THXM02.
[11] Youhei Morita and KEK Public Relations Office, https://www2.kek.jp/en/press/2009/KEKBluminosity2.html.
[12] K. Ohmi, R. Tomás, Y. Funakoshi, R. Calaga, T. Ieiri, Y. Morita, K. Nakanishi, K. Oide, Y. Ohnishi, Y. Sun, M. Tobiyama, F. Zimmermann, Response of colliding beam-beam system to harmonic excitation due to crab-cavity rf phase modulation, Phys. Rev. ST Accel. Beams 14 (2011) 111003.
[13] L. Carver, et al., First machine developments result with HL-LHC crab cavities in the SPS, in: Proc. 10th International Particle Accelerator Conference (IPAC'19), Melbourne, Australia, 19-24 2019, Geneva, Switzerland, 2019, pp. 338–341, http://dx.doi.org/10.18429/JACoW-IPAC2019-MOPGW094.
[14] R. Calaga, et al., First demonstration of the use of crab cavities on hadron beams, Phys. Rev. Accel. Beams 24 (2021) 062001.
[15] F. Antoniou, A. Alekou, H. Bartosik, T. Bohl, R. Calaga, L. Carver, J. Repond, G. Vandoni, Emittance growth in coast in the SPS at CERN, J. Phys. Conf. Ser. 1067 (2018) 022008.
[16] A. Alekou, F. Antoniou, H. Bartosik, R. Calaga, Emittance growth in coast in the SPS, 2017, pp. 107–112.
[17] A. Alekou, et al., SPS studies in preparation for the crab cavity experiment, in: Proc. of International Particle Accelerator Conference (IPAC'17), Copenhagen, Denmark, 2017, Geneva, Switzerland, 2017, pp. 2133–2135, http://dx.doi.org/10.18429/JACoW-IPAC2017-TUPVA034.
[18] P. Baudrenghien, T. Mastoridis, Transverse emittance growth due to rf noise in the high-luminosity LHC crab cavities, Phys. Rev. ST Accel. Beams 18 (2015) 101001.
[19] P. Sun, R. Assmann, R. Tomás, F. Zimmermann, Crab dispersion and its impact on the CERN Large Hadron Collider collimation, Phys. Rev. Spec. Top. Accel. Beams 13 (2010) 031001.
[20] D. Brett, R. Appleby, R. De Maria, J. Garcia, R. Garcia, B. Hall, G. Burt, Accurate crab cavity modeling for the high luminosity large hadron collider, Phys. Rev. Spec. Top. Accel. Beams 17 (2014) 104001.
[21] Y. Papaphilippou, Detecting chaos in particle accelerators through the frequency map analysis method, Chaos 24 (2014) 024412.
[22] J. Laskar, Hamiltonian Systems with Three Or more Degrees of Freedom, Springer, 1999, pp. 134–150.
[23] J. Laskar, Frequency map analysis and particle accelerators, in: Proceedings of the 2003 Particle Accelerator Conference, 2003, pp. 378–382.
[24] J. Laskar, Application of frequency map analysis, in: The Chaotic Universe: Proceedings of the Second ICRA Network Workshop, Rome, Pescara, Italy, 1-5 1999, 2000, p. 115.
[25] S. Kostoglou, H. Bartosik, Y. Papaphilippou, G. Sterbini, N. Triantafyllou, Tune modulation effects in the high luminosity large hadron collider, 2020.
[26] L. Deniau, H. Grote, G. Roy, F. Schmidt, many other contributors, MADX. Available at http://mad.web.cern.ch/mad/.
[27] E. McIntosh, F. Schmidt, R. De Maria, SixTrack - 6D Tracking Code.
[28] R. De Maria, M. Giovannozzi, Private communication.
[29] A. Latina, R. De Maria, RF multipole implementation, 2012.
[30] A. Alekou, Available at https://indico.cern.ch/event/806877/contributions/3361012/attachments/1825169/2990794/BBLumiMeeting_Alekou.pdf.
[31] M. Carlà, A. Alekou, H. Bartosik, L. Carver, Proceedings, 10th International Particle Accelerator Conference, Melbourne, Australia, 2019, MOPTS090.
[32] M. Carlà, A. Alekou, H. Bartosik, L. Carver, Beam-based measurement of the skew-sextupolar component of the radio frequency field of a HL-LHC-type crab-cavity, in: 10th International Particle Accelerator Conference, 2019, MOPTS090.
[33] A. Riche, Updated measured magnetic properties of the SPS magnets 363 MBA, 391 MBB, 108 QF, 106 QD, 1976.
[34] R. Tomás, G. Arduini, R. Calaga, A. Faus-Golfe, G. Rumolo, F. Zimmermann, Improved algorithms to determine the non-linear optics model of the SPS from non-linear chromaticity, 2007.
[35] M. Carlà, H. Bartosik, M. Beck, K. Li, M. Schenk, Proceedings, 9th International Particle Accelerator Conference (IPAC 2018): Vancouver, BC Canada, April 29-May 4, 2018, 2018, TUPAF022.
[36] M. Gasior, R. Jones, High sensitivity tune measurement by direct diode detection, 2005.
[37] P. Baudrenghien, K. Brodzinski, R. Calaga, O. Capatina, E. Jensen, A. Macpherson, E. Montesinos, V. Parma, Functional specifications of the LHC prototype crab cavity system, 2013.
[38] CERN optics repository: /afs/cern.ch/eng/lhc/optics/HLLHCV1.0.
[39] CERN optics repository: /afs/cern.ch/eng/lhc/optics/HLLHCV1.3.
[40] N. Karastathis, Y. Papaphilippou, Beam-beam simulations for optimizing the performance of the high-luminosity large hadron collider proton physics, 2020.